ACS Catalysis
Research Article
Cite This: ACS Catal. 2019, 9, 7090−7098
pubs.acs.org/acscatalysis

Impact of Transition Metal Carbide and Nitride Supports on the Electronic Structure of Thin Platinum Overlayers

Aaron Garg,[†] Danielle S. Gonçalves,[‡] Yusu Liu,[⊥] Zhenshu Wang,[†] Linxi Wang,[‖] Jong Suk Yoo,[§] Alexie Kolpak,[§] Robert M. Rioux,[‖,¶] Daniela Zanchet,[*,‡] and Yuriy Román-Leshkov[*,†]

[†]Department of Chemical Engineering, [⊥]Department of Materials Science and Engineering, and [§]Department of Mechanical Engineering, Massachusetts Institute of Technology, Cambridge, Massachusetts 02139, United States

[‡]Institute of Chemistry, University of Campinas, Campinas, SP 13083-970, Brazil

[‖]Department of Chemical Engineering and [¶]Department of Chemistry, The Pennsylvania State University, University Park, Pennsylvania 16802, United States

Ⓢ *Supporting Information*

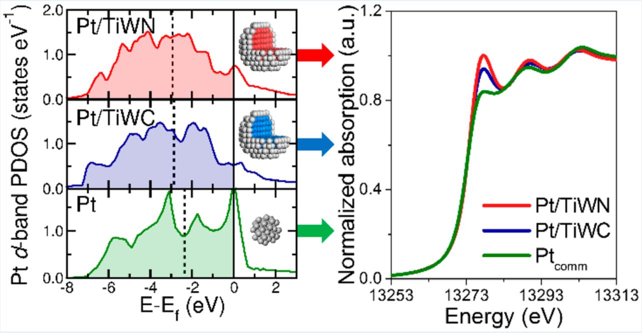

ABSTRACT: Atomically thin platinum (Pt) shells on titanium tungsten carbide (TiWC) and titanium tungsten nitride (TiWN) core nanoparticles display substantially modified catalytic performance compared to commercial Pt nanoparticles. In situ X-ray absorption near edge structure (XANES) and extended X-ray absorption fine structure (EXAFS) analyses indicate these differences are primarily caused by ligand effects from the hybridization of Pt and W d states at the core−shell interface. The heterometallic bonding between the shell and the core elements leads to broadening of the Pt valence d-band, a downshift of the d-band center, and greatly reduced adsorbate binding energies, as verified by density functional theory calculations and microcalorimetry of CO adsorption. In situ XANES measurements during reduction treatment demonstrated how surface oxides disrupt the bonding interactions between Pt and W. Changes to the Pt electronic structure from different core materials correlated with ethylene hydrogenation reactivity, where increased Pt d-band broadening was associated with weaker adsorbate binding and consequently lower turnover frequency. The significant electronic structure modification of Pt by the TiWC and TiWN cores exemplifies how core−shell nanoparticle architectures can be used to tune catalyst reactivity.

KEYWORDS: *tungsten carbide, core−shell nanoparticles, electronic structure, ethylene hydrogenation, in situ XAS, nitrides, platinum*

INTRODUCTION

Heterometallic core−shell catalysts comprising several monolayers (ML) of a noble metal coated on a core made of a different material feature unique properties, including enhanced catalytic performance and increased stability.[1−6] Improvements in catalytic activity can often be linked to changes in the geometry or electronic structure of the overlayer as a result of strain and ligand effects.[7−12] While early transition metal carbides and nitrides have been widely studied as standalone catalysts or as supports for nanoparticle-based catalysts for various reactions,[13−24] they are also ideal core materials for supporting noble metal shell catalysts owing to their earth abundance, thermal and chemical stability, and intrinsic ability to bind strongly to noble metals while still being immiscible with them.[25,26]

Recently, we demonstrated a versatile method for the synthesis of atomically thin Pt shells on titanium tungsten carbide (Pt/TiWC) and titanium tungsten nitride (Pt/TiWN) core nanoparticles (NPs) via a high-temperature self-assembly process.[26−28] These core−shell materials exhibit notably altered catalytic behavior compared to pure Pt NPs, including extremely high sinter-resistance,[26] enhanced tolerance to CO,[27] and increased selectivity in the partial hydrogenation of acetylene.[29] However, the origins of these changes in performance are not fully understood. While density functional theory (DFT) calculations can help elucidate structure−activity relationships using various hypothesized surface models, in situ characterization is needed to ensure accurate representation of the structure under reaction conditions where surface properties may differ significantly from the as-prepared materials.

Herein, we employed in situ X-ray absorption near edge structure (XANES) and extended X-ray absorption fine structure (EXAFS) to elucidate changes to both the electronic and geometric structure of Pt resulting from its interactions with the core. Specifically, Pt L_2-edge XANES measurements

Received: March 28, 2019
Revised: June 18, 2019
Published: June 28, 2019

DOI: 10.1021/acscatal.9b01272
ACS Catal. 2019, 9, 7090−7098

probing the unoccupied states in the Pt valence d-band and fitting of the EXAFS spectra to obtain structural parameters, including Pt−Pt distances and coordination numbers, were used to reveal the features responsible for altering catalytic performance. These analyses point to a broadened Pt d-band arising from heterometallic bonding with the core accompanied by weakened adsorbate binding. DFT calculations, microcalorimetry of CO adsorption, and ethylene hydrogenation reactivity were used to further investigate the observed modifications in the Pt d-band projected density of states (PDOS) and adsorbate binding energies for the core−shell materials relative to pure Pt. Additionally, in situ XANES and EXAFS characterization during reducing heat treatments allowed for examination of the effect of surface oxides on the material properties. The results yield fundamental insight into how TiWC and TiWN cores alter the properties of Pt, which will guide the design of improved catalysts.

■ RESULTS AND DISCUSSION

Modifications of the Pt electronic structure were investigated by examining changes in the Pt L_2-edge XANES spectra among the different materials and treatment conditions. It is known that the intensity of the absorption peak at the top of the rising edge (the "white line") in the XANES spectra is a direct probe of the unoccupied d PDOS and can provide details about the valence d-band above the Fermi level.[30] Ideally, both the Pt L_3 ($2p_{3/2} \rightarrow 5d_{5/2}, 5d_{3/2}$) and L_2-edges ($2p_{1/2} \rightarrow 5d_{3/2}$) should be measured to provide a complete picture of the 5d states,[31] but due to the proximity of the Pt L_3-edge to the W L_2-edge, this was not possible for these materials. The spin−orbit interaction leads to large differences between the L_3 and L_2 absorption edges,[32] and L_3 transitions are more favored by selection rules than L_2 transitions.[30] However, many good examples can be found in the literature where the Pt L_2-edge has produced the correct trends in the electronic structure.[32−35]

First, to eliminate varying degrees of surface Pt oxidation as a possible confounding effect and to study the catalysts as they would exist under reducing reaction conditions, carbon-supported Pt/TiWC and Pt/TiWN core−shell NPs (Ti:W ratio ca. 10:90) with 2 monolayers (ML) of Pt (denoted as $Pt_{2\,ML}$/TiWC and $Pt_{2\,ML}$/TiWN), as well as commercial carbon-supported Pt NPs (denoted as Pt_{comm}) were reduced under H_2 up to 300 °C. During this process, in situ XANES measurements of the Pt L_2-edge revealed how the white line intensity changed for each material as surface oxides were removed. Compared to metallic Pt^0 which has fully occupied $5d_{3/2}$ states,[30] PtO_2 has a fairly high white line due to the formation of unoccupied antibonding states above the Fermi level when Pt bonds with O. Accordingly, the white line intensity is expected to decrease as the Pt oxides are reduced to Pt^0. Initially, the three samples ($Pt_{2\,ML}$/TiWC, $Pt_{2\,ML}$/TiWN, and Pt_{comm}) showed white lines higher than the Pt standard but lower than PtO_2 (Figure 1). For Pt_{comm}, the white line was almost halfway in between both standards, corresponding to a large amount of surface oxide(s) as expected from its small average Pt NP size of 2.1 nm. After reduction, the white line intensity for Pt_{comm} decreased substantially, matching much more closely with that of the metallic Pt standard. The remaining difference can be attributed to nanoparticle size effects on the band structure and the relatively weak adsorption of H accompanied by the formation of Pt−H antibonding states.[32]

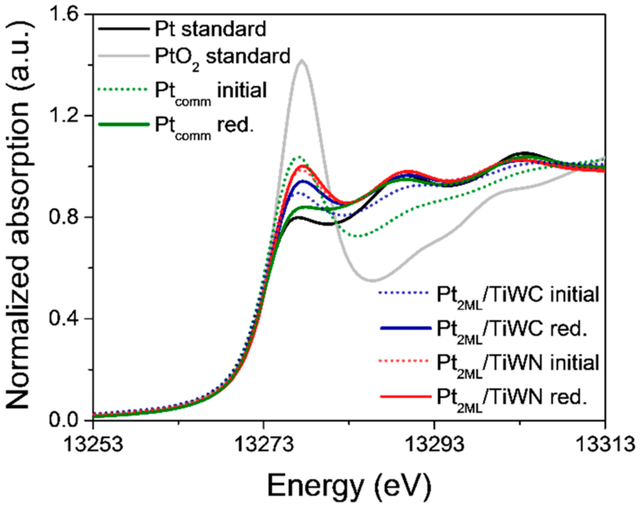

Figure 1. Comparison of Pt L_2-edge XANES spectra for Pt_{comm}, $Pt_{2\,ML}$/TiWC, and $Pt_{2\,ML}$/TiWN initially and after reduction under H_2 at 300 °C.

In contrast, $Pt_{2\,ML}$/TiWC and $Pt_{2\,ML}$/TiWN showed an opposite trend with slight increases in the white line intensity after the reduction treatment (Figure 1), indicating an increase in unoccupied $5d_{3/2}$ states for the core−shell materials compared to Pt_{comm}. This unusual phenomenon is likely related to the interaction with the TiWC and TiWN cores. We note this effect does not necessarily indicate a decrease in the total Pt d-band filling from a net charge transfer since the $5d_{5/2}$ PDOS was not measured and could have an equivalent or greater decrease in unoccupied states. Indeed, Kitchin et al. showed for bimetallic surfaces the change in d-band filling is typically negligible (less than 2% in magnitude),[7] suggesting the increase in unoccupied $5d_{3/2}$ states would be counterbalanced by a decrease in unoccupied Pt $5d_{5/2}$ states. Based on the work function of Pt,[36] WC,[37] and W_2N,[38] it is also expected that Pt in the core−shell materials would gain rather than lose charge, thus pointing to a more complex scenario involving geometric effects, ligand effects, or a combination of both as the cause for the observed phenomena rather than interatomic charge transfer.[8]

Possible changes in the Pt geometric structure for $Pt_{2\,ML}$/TiWC and $Pt_{2\,ML}$/TiWN were determined by in situ EXAFS (Figure 2). Given the lattice mismatch between fcc Pt (0.39 nm) and either fcc TiWC (0.42 nm) or fcc TiWN (0.41 nm),[27] a tensile strain on Pt might be expected when configured as a shell around these cores. However, the structural parameters obtained from the fitting of the EXAFS spectra (details of the fitting methodology provided in the Experimental Section) reveal that the Pt−Pt distance, r_{Pt-Pt}, for both $Pt_{2\,ML}$/TiWC and $Pt_{2\,ML}$/TiWN after reduction is nearly identical to that of Pt_{comm} (Table 1). This indicates the atomic arrangement of the Pt overlayer for these materials is nonepitaxial since the Pt does not adopt the crystal structure of the underlying substrate, and thus, lattice strain does not contribute to the observed changes in electronic structure. The nonepitaxial arrangement of Pt has been observed experimentally in other core−shell systems[39,40] and computationally using a heat, quench, and exfoliation (HQE) method that mimics the high-temperature self-assembly synthesis process to obtain the most energetically stable configurations.[41] Furthermore, the first-shell Pt−Pt coordination number, N_{Pt-Pt}, is

DOI: 10.1021/acscatal.9b01272
ACS Catal. 2019, 9, 7090−7098

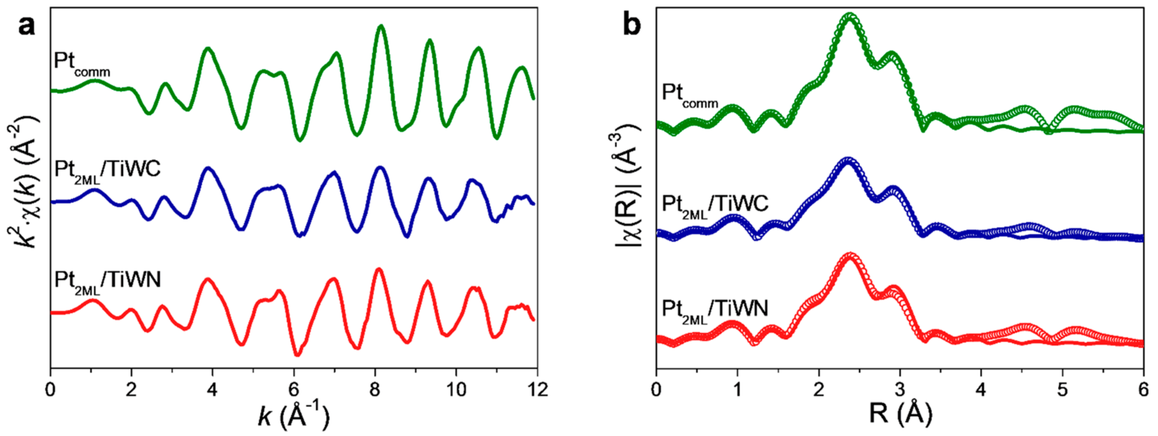

Figure 2. (a) Pt L_2-edge EXAFS oscillations, $k^2 \cdot \chi(k)$, for Pt$_{comm}$, Pt$_{2\ ML}$/TiWC, and Pt$_{2\ ML}$/TiWN after reduction under H_2 at 300 °C. (b) Fourier transform of the EXAFS oscillations (open circles), $|\chi(R)|$, and corresponding first-shell fits (solid lines).

Table 1. Structural Parameters Determined from the Pt L_2-Edge EXAFS Analysis after Reduction under H_2 at 300 °C

	Pt$_{comm}$	Pt$_{2\ ML}$/TiWC	Pt$_{2\ ML}$/TiWN
ΔE_0 (eV)	6.9 ± 0.9	6.9 ± 0.8	7.2 ± 1.0
N_{Pt-Pt}	10.4 ± 1.2	9.2 ± 1.0	9.5 ± 1.3
r_{Pt-Pt} (Å)	2.770 ± 0.002	2.773 ± 0.002	2.781 ± 0.003
σ^2_{Pt-Pt} (Å^2)	0.006 ± 0.001	0.009 ± 0.001	0.008 ± 0.001
R-factor	0.013	0.014	0.022

also similar between Pt$_{comm}$ (10.4), Pt$_{2\ ML}$/TiWC (9.2), and Pt$_{2\ ML}$/TiWN (9.5). These results provide strong evidence that ligand effects arising from bonding interactions between the Pt shell and the TiWC or TiWN core, and not geometric effects, are responsible for the differences in the Pt L_2-edge XANES spectra and electronic properties. The increase in white line intensity for Pt$_{2\ ML}$/TiWC and Pt$_{2\ ML}$/TiWN after reduction can then be explained by a strengthening of the heterometallic bonding interaction as surface oxides are removed. In addition, Pt appears to interact more strongly with TiWN than with TiWC based on the white line intensities, which is also consistent with previously reported core-level shifts of Pt 4f and W 4f XPS binding energies for the core−shell materials.[27]

Based on these findings, we propose that broadening of the Pt d-band resulting from the hybridization of Pt and W d states is the cause of the increase in empty Pt 5d$_{3/2}$ states for Pt$_{2\ ML}$/TiWC and Pt$_{2\ ML}$/TiWN compared to Pt$_{comm}$. While it is possible that C or N may also influence the electronic properties of Pt, our previous DFT calculations demonstrated that Pt−W interactions are much more energetically favorable than Pt−C interactions.[26] According to the d-band model, d-band broadening occurs when there is an increase in the d orbital overlap, causing a larger splitting of the orbital energy levels.[42] Compared to Pt, W has a large coupling matrix element, which is a measure of the extent of the metal d states.[43] Thus, hybridization of the Pt and W d states would result in increased d orbital overlap for Pt and a consequently broadened d-band. The d-band model also states that upon changes in the bandwidth, the d-band center relative to the Fermi level should move higher or lower in energy in order to conserve the d-band filling, and in this case, broadening of the Pt d-band should cause a downshift of the d-band center.[42] Although the total d-band occupancy stays fairly constant, the relative filling between 5d$_{3/2}$ and 5d$_{5/2}$ states can change as a result of band broadening.[31] Assuming the spin−orbit coupling energy between the 5d$_{3/2}$ and 5d$_{5/2}$ states remains the same, the larger energy separation between the d orbitals in broadened d-bands should promote the filling of 5d$_{5/2}$ states and decrease the filling of 5d$_{3/2}$ states.[31] Thus, the increase in L_2-edge white line intensity should not be attributed to an overall increase in unoccupied d states, but rather to d-band broadening resulting in a lower 5d$_{3/2}$ occupancy and a higher 5d$_{5/2}$ occupancy. A schematic depicting the electronic modifications of such an idealized d-band model leading to the described phenomena is shown in Figure 3.

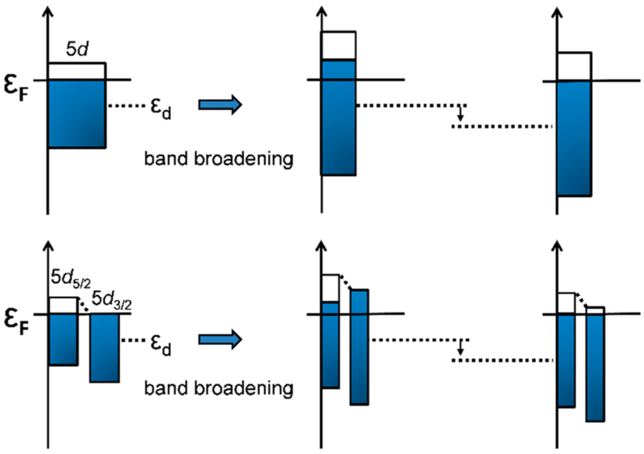

Figure 3. Schematic representation of changes to the Pt d-band electronic structure in Pt$_{2\ ML}$/TiWC and Pt$_{2\ ML}$/TiWN due to ligand effects. Hybridization of Pt and W states leads to Pt d-band broadening from increased d orbital overlap, a downshift in the d-band center to preserve the band filling, and a shift in the 5d$_{5/2}$ and 5d$_{3/2}$ occupancies.

The differences in the Pt L_2-edge white line intensity among Pt$_{comm}$, Pt$_{2\ ML}$/TiWC, and Pt$_{2\ ML}$/TiWN are directly related to differences in the Pt valence d-bandwidth and thus the d-band center, a key descriptor for adsorbate binding energies and catalytic reactivity.[42] Given the trend in white line intensities after reduction in Figure 1, we expect Pt$_{2\ ML}$/TiWN to have the broadest Pt d-band and the lowest d-band center, followed by Pt$_{2\ ML}$/TiWC and then Pt$_{comm}$. Accordingly, Pt$_{2\ ML}$/TiWN and Pt$_{2\ ML}$/TiWC should have weaker adsorbate binding energies than Pt$_{comm}$, demonstrating how carbide and nitride cores can be used to tune the catalytic properties of Pt. This effect was confirmed by microcalorimetry measurements of CO adsorption on these Pt surfaces at 25 °C. Whereas Pt_{comm} showed a large, exothermic initial heat of adsorption of 145 kJ mol^{-1} similar to values reported in literature,[44,45] no heat traces from CO adsorption were detected on either of the core−shell materials (Table S5). With a lower detection limit of ca. 20 kJ mol^{-1}, the lack of heat traces after introduction of CO into the system indicates significantly reduced CO binding energies for $Pt_{2\ ML}$/TiWC and $Pt_{2\ ML}$/TiWN. These results agree with in situ Pt L_2-edge XANES measurements of the samples under 10% CO/90% He flow at room temperature after reduction under H_2 (Figure 4). For Pt_{comm}, the strong adsorption of CO leads to additional antibonding states above the Fermi level and a considerable increase in the white line intensity.[33] By contrast, $Pt_{2\ ML}$/TiWC and $Pt_{2\ ML}$/TiWN both displayed virtually no change in their XANES spectra, providing further evidence that CO binding is greatly weakened due to the modified Pt electronic structure.

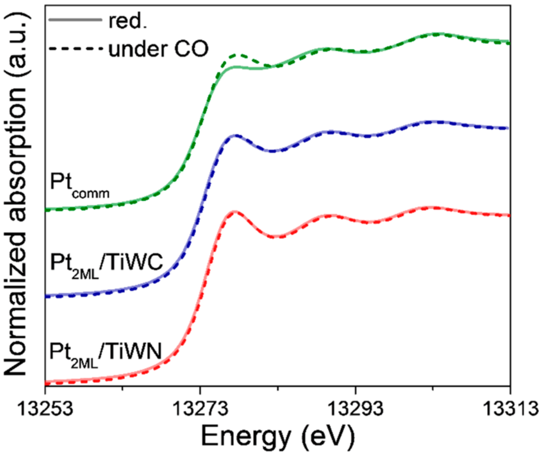

Figure 4. Pt L_2-edge XANES spectra for Pt_{comm}, $Pt_{2\ ML}$/TiWC, and $Pt_{2\ ML}$/TiWN after reduction under H_2 and followed by 10% CO/90% He flow at room temperature.

DFT calculations of Pt/TiWC and Pt/TiWN slabs were performed to corroborate the previous findings and to gain further insights into the changes in Pt electronic properties. Optimized models were derived from the HQE method (Figure 5a),[41] which were consistent with the Pt−Pt distances obtained from the EXAFS analysis (additional details in the Experimental Section). Due to the difficulty of converging the 2 ML Pt structures, only 1 ML Pt was modeled. PDOS calculations show the Pt d-band is significantly broadened for $Pt_{1\ ML}$/TiWC and $Pt_{1\ ML}$/TiWN compared to a pure Pt(111) surface as expected, leading to a downshift in the d-band center relative to the Fermi level (Figure 5b). $Pt_{1\ ML}$/TiWN has the lowest d-band center (−2.94 eV), followed by $Pt_{1\ ML}$/TiWC (−2.87 eV), and then Pt(111) (−2.37 eV), matching the trend suggested by the white lines in the Pt L_2-edge XANES spectra. Although the shifts in the d-band center will be attenuated for 2 ML Pt, these results still indicate a substantial weakening of adsorbate binding. Contour plots of the transferred charge density verified that there is a small charge transfer from W to Pt in agreement with the work functions (Figure 5c), and charge population analysis from the integrated PDOS indicated the overall filling of Pt d states actually increases slightly for both $Pt_{1\ ML}$/TiWC and $Pt_{1\ ML}$/TiWN (Figure 5d). These data confirmed that the increase in unoccupied Pt $5d_{3/2}$ states observed by XANES is a consequence of d-band broadening rather than interatomic charge transfer or even intra-atomic charge transfer from d to sp states.

While the general trends shown by the experiments and DFT are the same, EXAFS analysis of the W L_3-edge indicated the presence of surface W oxides (Table S8) as the reduction temperature of 300 °C was not high enough to completely reduce them,[46] a factor not considered in the previous DFT models. Although covered by Pt, the surface of TiWC and TiWN may have been oxidized through pinholes or inhomogeneities in the Pt shell, and these W oxides could disrupt the heterometallic bonding interactions between Pt and W and lessen the Pt d-band broadening caused by hybridization of their d states. Additional DFT calculations predicted fairly strong oxygen binding energies for both TiWC (−5.38 eV) and TiWN (−3.72 eV) cores and showed that an oxygen atom intercalated between the Pt overlayer and either TiWC or TiWN resulted in a slightly less downshifted Pt d-band center compared to the model without oxygen (Table 2). While the d-band center was still significantly lower than that of pure Pt(111), these results imply that the ligand effect causing the broadening of the Pt d-band and downshift of the d-band center was reduced due to the presence of W oxides.

To investigate the effect of removing surface W oxides on the Pt electronic structure as evidenced by the Pt L_2-edge white line intensity, $Pt_{2\ ML}$/TiWC was recarburized under 20% CH_4/80% H_2 flow up to 600 °C. Analysis of the in situ W L_3-edge EXAFS spectra after recarburization confirmed that W oxides were depleted and that the recarburized TiWC core features matched closely with those of an unoxidized carbide structure (Figure S4). In addition, the Pt L_2-edge EXAFS analysis demonstrated that the Pt geometric structure remained the same after recarburization (Figure S6). However, the intensity of the Pt L_2-edge white line increased considerably (Figure 6a), supporting the hypothesis that surface W oxidation weakened the interaction between the Pt shell and the TiWC core. In fact, the Pt L_2-edge white line for recarburized $Pt_{2\ ML}$/TiWC (no W oxides) slightly surpassed that of $Pt_{2\ ML}$/TiWN (with surface W oxides). Although in situ XANES measurements with a high-temperature treatment to remove W oxides in $Pt_{2\ ML}$/TiWN were not conducted, we would expect a similar effect causing its white line to increase beyond that of recarburized $Pt_{2\ ML}$/TiWC.

These alterations in Pt electronic properties due to different core materials and thermal treatments were clearly demonstrated using ethylene hydrogenation as a probe reaction. As shown in Figure 6, the downshift in the d-band center associated with increasing Pt L_2-edge white line intensities resulted in progressively slower turnover frequencies (TOFs).[47] These reactions were performed at 45 °C under differential conditions in the absence of heat and mass transfer limitations. Reaction rates for all samples were normalized by the number of surface sites quantified using electrochemical hydrogen underpotential deposition (Table S10). Of the samples reduced below 300 °C, Pt_{comm} showed the highest TOF for ethylene hydrogenation (7.1 s^{-1}), followed by $Pt_{2\ ML}$/TiWC (4.7 s^{-1}), and then $Pt_{2\ ML}$/TiWN (0.9 s^{-1}) (Figure 6b). We posit that the lower TOFs for the core−shell materials arose from the weakened binding of ethylene and hydrogen and the consequently lower surface coverage of adsorbates. For $Pt_{2\ ML}$/TiWC and $Pt_{2\ ML}$/TiWN treated at 600 °C, the TOF decreased substantially to 0.2 and 0.02 s^{-1}, respectively, suggesting even weaker adsorbate binding due to a more

DOI: 10.1021/acscatal.9b01272
ACS Catal. 2019, 9, 7090−7098

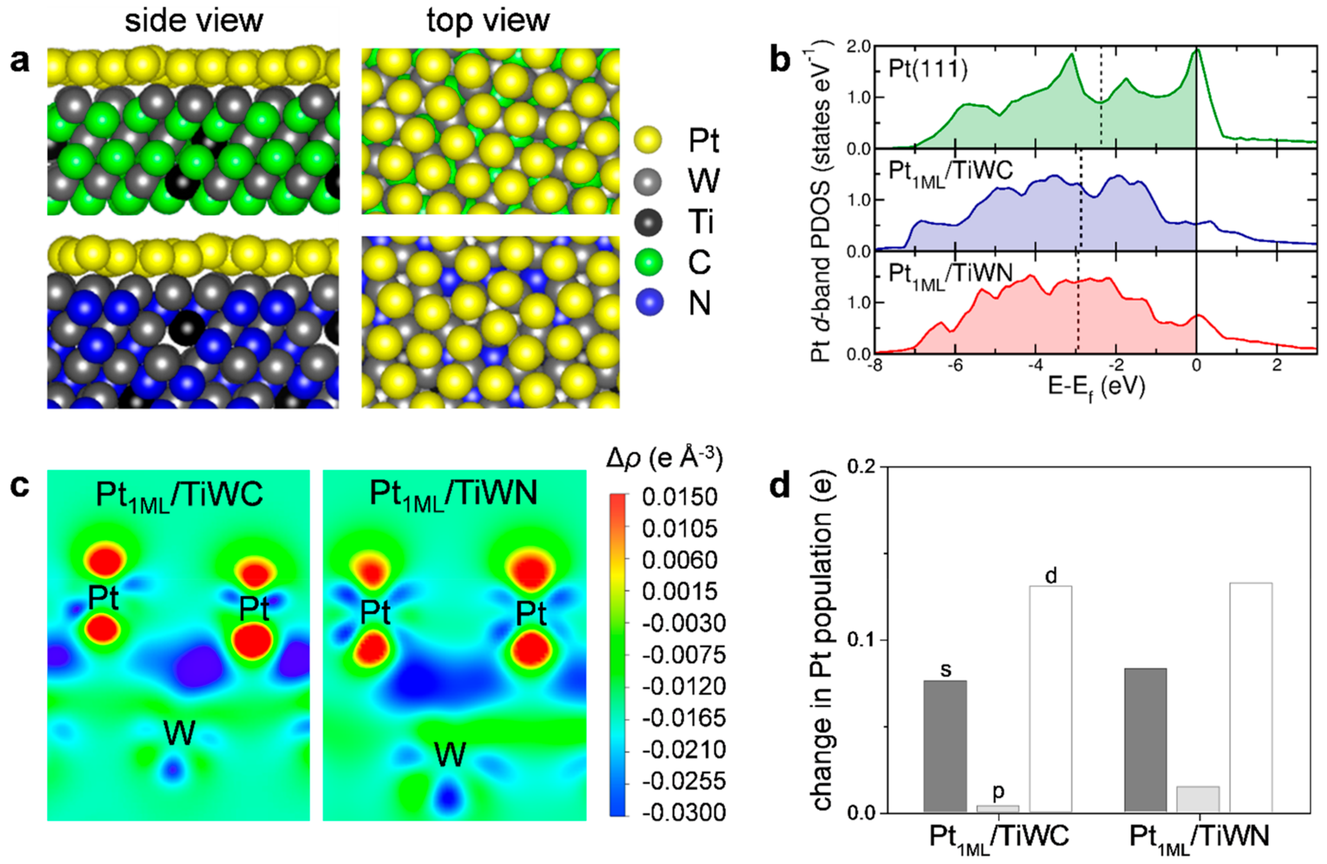

Figure 5. (a) Representative slab models for $Pt_{1\ ML}/TiWC$ (top) and $Pt_{1\ ML}/TiWN$ (bottom) used in DFT calculations. (b) Calculated Pt valence d-band PDOS and d-band centers aligned to the Fermi level energy. (c) Contour plots of interatomically transferred charge density between Pt and W in $Pt_{1\ ML}/TiWC$ and $Pt_{1\ ML}/TiWN$. (d) Change in Pt valence s, p, and d orbital populations for $Pt_{1\ ML}/TiWC$ and $Pt_{1\ ML}/TiWN$ relative to pure Pt calculated from the integrated PDOS.

Table 2. Pt *d*-Band Centers from DFT Calculations Comparing with and without an Oxygen Atom Intercalated between the Pt Overlayer and Either TiWC or TiWN

	Pt d-band center (eV)	
material	without O	with O intercalated
Pt(111)	−2.37	–
$Pt_{1\ ML}/TiWC$	−2.87	−2.82 (−2.72[a])
$Pt_{1\ ML}/TiWN$	−2.94	−2.87 (−2.84[a])

[a] Pt d-band center for the three Pt atoms closest to the oxygen atom.

downshifted Pt d-band center upon removal of W oxides. This effect is consistent with the considerable increase in the Pt L_2-edge white line intensity for $Pt_{2\ ML}/TiWC$ after recarburization at 600 °C. These trends in TOF for ethylene hydrogenation further verify how surface W oxides disrupt the heterometallic bonding interactions that lead to the modification of the Pt shell electronic structure.

CONCLUSIONS

We have shown with Pt L_2-edge XANES measurements the significantly altered electronic structure of Pt shells on TiWC and TiWN core NPs. The XANES spectra indicated an increase in unoccupied Pt $5d_{3/2}$ states, which was attributed to a broadened d-band. EXAFS analysis, however, revealed Pt−Pt distances nearly identical to that of pure Pt NPs. Consequently, these electronic modifications were determined to be the result of ligand effects arising from the hybridization of Pt and W d states rather than strain effects. Broadening of the Pt d-band was accompanied by a downshift of the d-band center, as demonstrated by DFT, and this led to substantially reduced adsorbate binding energies, as verified by the CO microcalorimetry measurements. Surface W oxidation was found to weaken the heterometallic bonding interactions between Pt and W, leading to a less modified Pt electronic structure than without oxygen. The differences in the electronic properties of Pt also translated into differences in reactivity for ethylene hydrogenation, illustrating the ability of the core material to tune the catalytic activity of Pt, with potential applications for selective hydrogenation. In addition to providing fundamental insight into the unique behavior of these promising core−shell materials, these results demonstrate the importance of detailed physical characterization of the structure for accurate prediction of material properties and the utility of in situ methods for correlation with reactivity.

EXPERIMENTAL SECTION

Materials Synthesis. $Pt_{2\ ML}/TiWC$ and $Pt_{2\ ML}/TiWN$ core−shell NPs (Ti:W ratio ca. 10:90, particle size ca. 7 nm) were synthesized using methods previously reported by our group.[26,27] Although we observe some nonuniformity in the monolayer thickness due to experimental variability, based on our previous theoretical calculations demonstrating that the subsurface carbide does not dictate the packing of surface-anchored Pt, we expect Pt to cover all facets of the TiWC and TiWN NPs.[41] Briefly, silica-encapsulated titanium tungsten

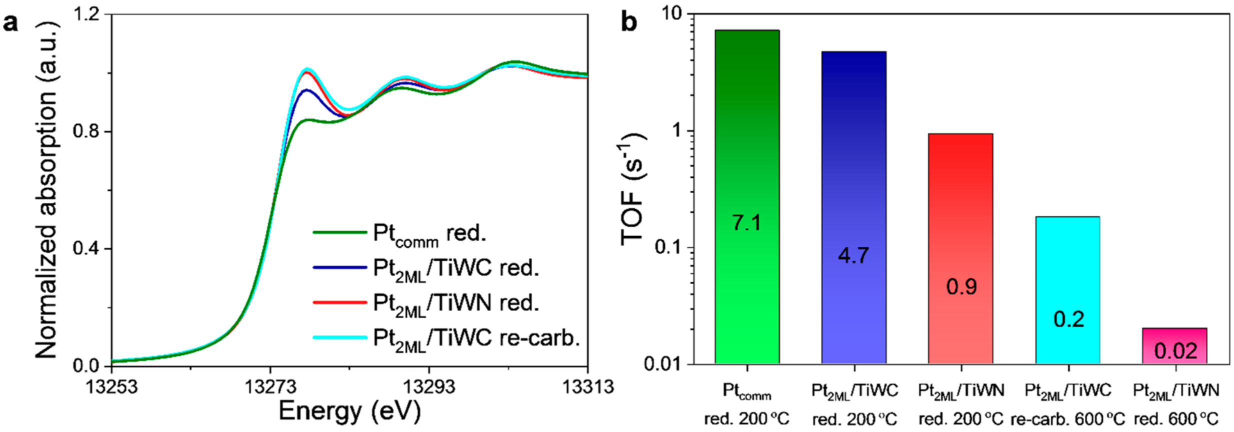

Figure 6. (a) Pt L_2-edge XANES spectra for Pt$_{comm}$, Pt$_{2\ ML}$/TiWC, and Pt$_{2\ ML}$/TiWN after reduction under H_2 at 300 °C and Pt$_{2\ ML}$/TiWC after recarburization under CH_4/H_2 at 600 °C. (b) TOF for ethylene hydrogenation at 45 °C with C_2H_4:H_2 ratio = 1:1 after sample pretreatment by reduction under H_2 or recarburization under CH_4/H_2.

oxide NPs coated with a Pt salt (denoted as $SiO_2/(NH_4)_2PtCl_6/Ti_{0.1}W_{0.9}O_x$) were prepared using a reverse microemulsion (RME) method by mixing *n*-heptane, Brij-L4 surfactant, ultrapure water (18 MΩ•cm), NH_4OH solution, tungsten isopropoxide, and titanium isopropoxide at room temperature. The mixture was stirred for 4 h to allow the $Ti_{0.1}W_{0.9}O_x$ NPs to form. Afterward, a separate RME containing *n*-heptane, Brij-L4, and chloroplatinic acid dissolved in water was added dropwise to the first RME causing the precipitation of the Pt salt onto the $Ti_{0.1}W_{0.9}O_x$ NPs. After another 4 h, tetraethyl orthosilicate was added and left to react for 16.5 h, encapsulating the particles in a SiO_2 shell. Then, methanol was added to precipitate the $SiO_2/(NH_4)_2PtCl_6/Ti_{0.1}W_{0.9}O_x$ NPs, which were recovered after centrifugation and washing with acetone. SiO_2/Pt/TiWC core−shell particles were formed by heating the oxide powder up to 900 °C at a ramp rate of 2 °C min^{-1} under a gas flow of 20% CH_4/80% H_2 and holding for 5 h. After cooling to room temperature under H_2, the samples were passivated using 1% O_2/99% N_2 flow. The SiO_2 was removed by dissolution in a mixture of degassed ethanol and aqueous HF solution for 18 h at room temperature with dispersed carbon black added as a support. The Pt/TiWC/C NPs (ca. 30 wt % core−shell particles) were recovered through centrifugation, washed thoroughly with degassed ethanol and water, and dried under vacuum. To synthesize Pt/TiWN/C, the Pt/TiWC/C powder was heated up to 800 °C at a ramp rate of 2 °C min^{-1} under NH_3 flow and held for 3 h. After cooling to room temperature under NH_3, the samples were passivated. Complete synthetic details are provided in ref 27.

Characterization. Basic characterization data of the materials are provided in the Supporting Information, while a complete determination of the core−shell structure is shown in refs 26 and 27. Powder X-ray diffraction (PXRD) was performed on a Bruker D8 diffractometer using Cu Kα radiation with a step size of 0.02° and step time of 0.2 s. Transmission electron microscopy (TEM) was performed on a JEOL 2010F equipped with a field emission gun operating at 200 kV. X-ray photoelectron spectroscopy (XPS) was performed on a PHI Versaprobe II with a monochromatic aluminum anode X-ray source operating at 50 W and 15 kV. Sample elemental composition was measured on an Agilent 7900 ICP-MS. X-ray absorption spectroscopy (XAS) measurements of the Pt L_2-edge (13,273 eV) and W L_3-edge (10,207 eV) were performed at the 12-BM-B beamline at the Advanced Photon Source (APS) at Argonne National Laboratory. It was not possible to extract information from the Pt L_3-edge (11 564 eV) for this system due to the proximity to the W L_2-edge (11 544 eV).

The in situ XAS measurements were performed in transmission mode using undiluted samples loaded into 1 mm quartz capillaries and packed between two plugs made of quartz wool. Heating was provided by two Kanthal wire resistors wound around a ceramic block placed below the sample, and the temperature was measured by a thermocouple inserted into the capillary as close as possible to the sample without contact. Initial XAS measurements were taken under He flow. Reductions were carried out under pure H_2 up to 300 °C at a ramp rate of 2 °C min^{-1} followed by cooling to room temperature under H_2 flow. After reduction, 10% CO/90% He at room temperature was flowed over the samples. Pt$_{2\ ML}$/TiWC was recarburized under 20% CH_4/80% H_2 flow up to 600 °C at a ramp rate of 5 °C min^{-1} followed by cooling to room temperature.

Pt or W foils were measured simultaneously with the samples, and the reference spectra were used to align the energies. Bulk Pt, W, WC, W_2C, W_2N, WO_2, and WO_3 were used as standards. The data were analyzed using the Demeter 0.9.23 software package following the standard practices.[48] For the EXAFS data analysis, the amplitude reduction factors (S_0^2) were constrained from the standards, and the coordination numbers (N), interatomic distances (r), Debye−Waller factors (σ^2), and edge energy corrections (ΔE_0) were fitted from the data. EXAFS spectra were fitted using multiple k-weights of 1, 2, and 3 and a Hanning window. The minimum wavenumber, k_{min}, was limited to 2.5 Å^{-1} due to high sensitivity to the background subtraction below this value. For the W L_3-edge, the maximum wavenumber, k_{max}, was chosen based on the quality of the $k^2 \cdot \chi(k)$ spectra at high k. For the Pt L_2-edge, the k_{max} was limited to ∼11 Å^{-1} by the Pt L_1-edge at 13 880 eV. Other scattering models were also tested, which did not significantly improve the fit quality or impact the overall trend. Due to the low concentration of Ti atoms, their presence was not considered in the fit, and any effects of Ti on the electronic structure should be small relative to W. Attempts to include a Pt−W path were not successful due to the limited k_{max} and the close atomic numbers of Pt and W, which resulted in a high correlation with Pt−Pt or W−W paths. The addition of first-shell oxide paths improved most fits at low *R*. However, we note for $Pt_{2\ ML}$/TiWC and $Pt_{2\ ML}$/TiWN samples at the W L_3-edge, it was not possible to clearly differentiate between light C, N, and O atoms.

Microcalorimetry Measurements. The uptake and heat of adsorption of CO were measured in a combined breakthrough reactor (BTR)−differential scanning calorimetry (DSC)−mass spectrometer (MS) instrument. The DSC controlled the temperature of the catalyst bed and recorded transient heat flow, while the MS was used to detect the breakthrough of CO indicating catalyst saturation. Catalysts were placed between two pieces of quartz wool in a quartz tube (1/4 in O.D.), which was inserted into the body of the DSC. An identical piece of quartz tubing was inserted into the reference side of the DSC. Prior to CO adsorption, the catalysts were pretreated under H_2 flow at 200 °C for 2 h. The sample bed was then purged with He for 4 h to remove H_2. Afterward, the BTR was cooled down to 25 °C for adsorption measurements. CO was diluted to 5.38% with Ar and filled a 50 μL sample loop. During each injection, CO adsorbed to the sample bed while Ar immediately broke through. Simultaneously, the DSC recorded the heat flow due to adsorption of CO. Pulses were spaced in 30 min intervals to allow enough time for complete adsorption and heat transfer. The quantity of adsorbed CO in each pulse was calculated from the difference between the mass spectrometer signal after sample breakthrough and the mass spectrometer signal associated with the concentration of CO in the sample loop, and the exothermic heat released during each pulse was determined by integration of the corresponding DSC peak. The heat of adsorption was then taken to be the exothermic heat divided by the uptake.

DFT Calculations. Spin-polarized calculations were performed using VASP[49] with PAW pseudopotentials[50] and the RPBE functional.[51] The Fast algorithm, Accurate precision, and 2 × 2 × 1 Monkhorst−Pack *k*-point mesh[52] were used for all Pt/TiWC and Pt/TiWN slab calculations with an energy cutoff of 520 eV and a Gaussian smearing of 0.1 eV. The periodic slab models for Pt/TiWC and Pt/TiWN were built using the methods outlined in ref 41 separated by more than 17 Å of vacuum perpendicular to the surface plane. Due to the difficulty of converging the 2 ML Pt structures owing to the high computational intensity of the HQE method, only 1 ML of Pt was modeled. The Pt layer along with the top 2 layers of TiWC or TiWN in the slab model and any adsorbates were allowed to relax until the forces on the individual relaxed atoms were less than 10^{-3} eV $Å^{-1}$. PDOS were calculated using a dense 9 × 9 × 1 Monkhorst−Pack *k*-point mesh for accuracy.

Catalytic Testing. The ethylene hydrogenation reactivity was measured in a packed bed flow reactor under differential conditions. The reactor temperature was kept constant by an Applied Test Systems (ATS) split furnace at 45 °C. The hydrogenation experiments were carried out with a total flow rate of 60 mL min^{-1} (C_2H_4 = 5 mL min^{-1}, H_2 = 5 mL min^{-1}, CH_4 = 5 mL min^{-1}, He = 45 mL min^{-1}). An Agilent 6890 Gas Chromatograph (GC) with flame ionization detector (FID) was used for product distribution analysis. A thermocouple was placed inside a 3/8 in. stainless steel tube (inner diameter: 0.305 in.), and quartz wool was set right above the thermocouple as a physical support of the catalyst bed with the reaction gas mixture flowing downward. Core−shell particles supported on carbon black were well mixed with α-alumina (100−200 mesh) to enhance heat transfer and loaded on top of the quartz wool in the reactor (Figure S7). The catalyst bed length was around 4.5 cm. The catalysts were activated by reducing under 50 mL min^{-1} H_2 up to 200 °C and holding for 30 min. To remove surface W oxides, the core−shell materials were pretreated at higher temperatures as follows. $Pt_{2\ ML}$/TiWC was recarburized under 35 mL min^{-1} H_2 and 15 mL min^{-1} CH_4 up to 600 °C and held for 2 h. $Pt_{2\ ML}$/TiWN was reduced under 50 mL min^{-1} H_2 up to 600 °C and held for 2 h. The reactions were free of mass and heat transfer limitations based on Mear's criteria calculations (Table S11). The TOFs were calculated under differential conditions (C_2H_4 conversion less than 10%) at 45 °C and were normalized by the number of Pt surface sites as quantified by electrochemical hydrogen underpotential deposition (H_{upd}) (Table S10).

■ ASSOCIATED CONTENT

Ⓢ Supporting Information

The Supporting Information is available free of charge on the ACS Publications website at DOI: 10.1021/acscatal.9b01272.

> Additional materials characterization; EXAFS fitting details, plots, and results; CO microcalorimetry measurements; discussion of W L_3-edge XANES; representative slab models for DFT calculations; reactor diagram; Pt surface areas and measurement details; reactor parameters and Mears criteria (PDF)

■ AUTHOR INFORMATION

Corresponding Authors

*E-mail: daniela@iqm.unicamp.br.
*E-mail: yroman@mit.edu.

ORCID

Robert M. Rioux: 0000-0002-6019-0032
Daniela Zanchet: 0000-0003-1475-2548
Yuriy Román-Leshkov: 0000-0002-0025-4233

Notes

The authors declare no competing financial interest.

■ ACKNOWLEDGMENTS

This work was supported by the U.S. Department of Energy, Office of Basic Energy Sciences (DE- SC0016214). D.S.G. and D.Z. acknowledge funding by the São Paulo Research Foundation (FAPESP 2015/23900-2 and 2015/50375-6) and the National Council of Technological and Scientific Development (CNPq 309373/2014-0 and D.S.G. Ph.D. scholarship CNPq 140547/2017-7). This study was also financed in part by the Coordination for the Improvement of Higher Education Personnel (CAPES)−Finance Code 001, Brazil. L.W. and R.M.R. acknowledge support from the Department of Energy, Office of Basic Energy Sciences, Chemical Sciences, and Biosciences Division, Catalysis Sciences Program under grant number DE-SC0016192. We thank the MISTI-Brazil grant for travel support. The authors thank T.E.R. Fiuza for her help during the XANES/EXAFS data collection. This research used resources of the Advanced Photon Source, a U.S. DOE, Office of Science User Facility operated for the DOE Office of Science by Argonne National Laboratory under Contract No. DE-AC02-06CH11357 (12-BM-B beamline, GUP 55290). Computations were performed using computational resources from the Extreme Science and Engineering Discovery Environment (XSEDE) and the

National Energy Research Scientific Computing Center (NERSC).

■ REFERENCES

(1) Hu, J.; Wu, L.; Kuttiyiel, K. A.; Goodman, K. R.; Zhang, C.; Zhu, Y.; Vukmirovic, M. B.; White, M. G.; Sasaki, K.; Adzic, R. R. Increasing Stability and Activity of Core-Shell Catalysts by Preferential Segregation of Oxide on Edges and Vertexes: Oxygen Reduction on Ti-Au@Pt/C. *J. Am. Chem. Soc.* **2016**, *138*, 9294−9300.

(2) Kelly, T. G.; Chen, J. G. Metal Overlayer on Metal Carbide Substrate: Unique Bimetallic Properties for Catalysis and Electrocatalysis. *Chem. Soc. Rev.* **2012**, *41*, 8021−8034.

(3) Strickler, A. L.; Jackson, A.; Jaramillo, T. F. Active and Stable Ir@Pt Core−Shell Catalysts for Electrochemical Oxygen Reduction. *ACS Energy Lett.* **2017**, *2*, 244−249.

(4) Oezaslan, M.; Hasché, F.; Strasser, P. Pt-Based Core−Shell Catalyst Architectures for Oxygen Fuel Cell Electrodes. *J. Phys. Chem. Lett.* **2013**, *4*, 3273−3291.

(5) Strasser, P.; Koh, S.; Anniyev, T.; Greeley, J.; More, K.; Yu, C.; Liu, Z.; Kaya, S.; Nordlund, D.; Ogasawara, H.; Toney, M. F.; Nilsson, A. Lattice-Strain Control of the Activity in Dealloyed Core-Shell Fuel Cell Catalysts. *Nat. Chem.* **2010**, *2*, 454−460.

(6) Luo, J.; Wang, L.; Mott, D.; Njoki, P. N.; Lin, Y.; He, T.; Xu, Z.; Wanjana, B. N.; Lim, I. I. S.; Zhong, C.-J. Core/Shell Nanoparticles as Electrocatalysts for Fuel Cell Reactions. *Adv. Mater.* **2008**, *20*, 4342−4347.

(7) Kitchin, J. R.; Norskov, J. K.; Barteau, M. A.; Chen, J. G. Role of Strain and Ligand Effects in the Modification of the Electronic and Chemical Properties of Bimetallic Surfaces. *Phys. Rev. Lett.* **2004**, *93*, 156801.

(8) Kitchin, J. R.; Norskov, J. K.; Barteau, M. A.; Chen, J. G. Modification of the Surface Electronic and Chemical Properties of Pt(111) by Subsurface 3d Transition Metals. *J. Chem. Phys.* **2004**, *120*, 10240−10246.

(9) Ghosh, T.; Vukmirovic, M. B.; DiSalvo, F. J.; Adzic, R. R. Intermetallics as Novel Supports for Pt Monolayer O2 Reduction Electrocatalysts: Potential for Significantly Improving Properties. *J. Am. Chem. Soc.* **2010**, *132*, 906−907.

(10) Kuttiyiel, K. A.; Sasaki, K.; Choi, Y.; Su, D.; Liu, P.; Adzic, R. R. Nitride Stabilized PtNi Core-Shell Nanocatalyst for High Oxygen Reduction Activity. *Nano Lett.* **2012**, *12*, 6266−6271.

(11) Tian, X.; Luo, J.; Nan, H.; Zou, H.; Chen, R.; Shu, T.; Li, X.; Li, Y.; Song, H.; Liao, S.; Adzic, R. R. Transition Metal Nitride Coated with Atomic Layers of Pt as a Low-Cost, Highly Stable Electrocatalyst for the Oxygen Reduction Reaction. *J. Am. Chem. Soc.* **2016**, *138*, 1575−1583.

(12) Wang, D.; Xin, H. L.; Wang, H.; Yu, Y.; Rus, E.; Muller, D. A.; DiSalvo, F. J.; Abruña, H. D. Facile Synthesis of Carbon-Supported Pd−Co Core−Shell Nanoparticles as Oxygen Reduction Electrocatalysts and Their Enhanced Activity and Stability with Monolayer Pt Decoration. *Chem. Mater.* **2012**, *24*, 2274−2281.

(13) Neylon, M. K.; Choi, S.; Kwon, H.; Curry, K. E.; Thompson, L. T. Catalytic Properties of Early Transition Metal Nitrides and Carbides: n-Butane Hydrogenolysis, Dehydrogenation and Isomerization. *Appl. Catal., A* **1999**, *183*, 253−263.

(14) Oyama, S. T. Preparation and Catalytic Properties of Transition Metal Carbides and Nitrides. *Catal. Today* **1992**, *15*, 179−200.

(15) Yu, C. C.; Ramanathan, S.; Dhandapani, B.; Chen, J. G.; Oyama, S. T. Bimetallic Nb−Mo Carbide Hydroprocessing Catalysts: Synthesis, Characterization, and Activity Studies. *J. Phys. Chem. B* **1997**, *101*, 512−518.

(16) Iglesia, E.; Baumgartner, J. E.; Ribeiro, F. H.; Boudart, M. Bifunctional Reactions of Alkanes on Tungsten Carbides Modified by Chemisorbed Oxygen. *J. Catal.* **1991**, *131*, 523−544.

(17) Ribeiro, F. H.; Dalla Betta, R. A.; Boudart, M.; Baumgartner, J.; Iglesia, E. Reactions of Neopentane, Methylcyclohexane, and 3,3-Dimethylpentane on Tungsten Carbides: The Effect of Surface Oxygen on Reaction Pathways. *J. Catal.* **1991**, *130*, 86−105.

(18) Patt, J.; Moon, D. J.; Phillips, C.; Thompson, L. Molybdenum Carbide Catalysts for Water−Gas Shift. *Catal. Lett.* **2000**, *65*, 193−195.

(19) Yang, M.; Cui, Z.; DiSalvo, F. J. Mesoporous Titanium Nitride Supported Pt Nanoparticles as High Performance Catalysts for Methanol Electrooxidation. *Phys. Chem. Chem. Phys.* **2013**, *15*, 1088−1092.

(20) Molinari, V.; Giordano, C.; Antonietti, M.; Esposito, D. Titanium Nitride-Nickel Nanocomposite as Heterogeneous Catalyst for the Hydrogenolysis of Aryl Ethers. *J. Am. Chem. Soc.* **2014**, *136*, 1758−1761.

(21) Murugappan, K.; Anderson, E. M.; Teschner, D.; Jones, T. E.; Skorupska, K.; Román-Leshkov, Y. Operando NAP-XPS Unveils Differences in MoO3 and Mo2C During Hydrodeoxygenation. *Nat. Catal.* **2018**, *1*, 960−967.

(22) Schweitzer, N. M.; Schaidle, J. A.; Ezekoye, O. K.; Pan, X.; Linic, S.; Thompson, L. T. High Activity Carbide Supported Catalysts for Water Gas Shift. *J. Am. Chem. Soc.* **2011**, *133*, 2378−2381.

(23) Saha, S.; Martin, B.; Leonard, B.; Li, D. Probing Synergetic Effects Between Platinum Nanoparticles Deposited via Atomic Layer Deposition and a Molybdenum Carbide Nanotube Support Through Surface Characterization and Device Performance. *J. Mater. Chem. A* **2016**, *4*, 9253−9265.

(24) Tan, S.; Wang, L.; Saha, S.; Fushimi, R. R.; Li, D. Active Site and Electronic Structure Elucidation of Pt Nanoparticles Supported on Phase-Pure Molybdenum Carbide Nanotubes. *ACS Appl. Mater. Interfaces* **2017**, *9*, 9815−9822.

(25) Zhong, Y.; Xia, X.; Shi, F.; Zhan, J.; Tu, J.; Fan, H. J. Transition Metal Carbides and Nitrides in Energy Storage and Conversion. *Adv. Sci.* **2016**, *3*, 1500286.

(26) Hunt, S. T.; Milina, M.; Alba-Rubio, A. C.; Hendon, C. H.; Dumesic, J. A.; Román-Leshkov, Y. Self-Assembly of Noble Metal Monolayers on Transition Metal Carbide Nanoparticle Catalysts. *Science* **2016**, *352*, 974−978.

(27) Garg, A.; Milina, M.; Ball, M.; Zanchet, D.; Hunt, S. T.; Dumesic, J. A.; Román-Leshkov, Y. Transition-Metal Nitride Core@Noble-Metal Shell Nanoparticles as Highly CO Tolerant Catalysts. *Angew. Chem., Int. Ed.* **2017**, *56*, 8828−8833.

(28) Hunt, S. T.; Milina, M.; Wang, Z.; Román-Leshkov, Y. Activating Earth-Abundant Electrocatalysts for Efficient, Low-Cost Hydrogen Evolution/Oxidation: Sub-Monolayer Platinum Coatings on Titanium Tungsten Carbide Nanoparticles. *Energy Environ. Sci.* **2016**, *9*, 3290−3301.

(29) Wang, Z.; Garg, A.; Wang, L.; He, H.; Dasgupta, A.; Zanchet, D.; Janik, M. J.; Rioux, R. M.; Román-Leshkov, Y. Enhancement of Alkyne Semi-Hydrogenation Selectivity by Electronic Modification of Platinum. Submitted.

(30) Brown, M.; Peierls, R. E.; Stern, E. A. White Lines in X-Ray Absorption. *Phys. Rev. B* **1977**, *15*, 738−744.

(31) Mansour, A. N.; Cook, J. W.; Sayers, D. E. Quantitative Technique for the Determination of the Number of Unoccupied d-Electron States in a Platinum Catalyst Using the L2,3 X-Ray Absorption Edge Spectra. *J. Phys. Chem.* **1984**, *88*, 2330−2334.

(32) Ramaker, D. E.; Mojet, B. L.; Garriga Oostenbrink, M. T.; Miller, J. T.; Koningsberger, D. C. Contribution of Shape Resonance and Pt−H EXAFS in the Pt L2,3 X-Ray Absorption Edges of Supported Pt Particles: Application and Consequences for Catalyst Characterization. *Phys. Chem. Chem. Phys.* **1999**, *1*, 2293−2302.

(33) Lei, Y.; Jelic, J.; Nitsche, L. C.; Meyer, R.; Miller, J. Effect of Particle Size and Adsorbates on the L3, L2 and L1 X-ray Absorption Near Edge Structure of Supported Pt Nanoparticles. *Top. Catal.* **2011**, *54*, 334−348.

(34) Kubota, T.; Asakura, K.; Ichikuni, N.; Iwasawa, Y. A New Method for Quantitative Characterization of Adsorbed Hydrogen on Pt Particles by Means of Pt L-Edge XANES. *Chem. Phys. Lett.* **1996**, *256*, 445−448.

(35) Notoya, Y.; Hayakawa, K.; Fujikawa, T.; Kubota, T.; Shido, T.; Asakura, K.; Iwasawa, Y. Multiple Scattering Approach to the Pt L2-

edge XANES of CO Adsorption on Small Pt Particles. *Chem. Phys. Lett.* **2002**, *357*, 365−370.

(36) Yan, H.; Tian, C.; Wang, L.; Wu, A.; Meng, M.; Zhao, L.; Fu, H. Phosphorus-Modified Tungsten Nitride/Reduced Graphene Oxide as a High-Performance, Non-Noble-Metal Electrocatalyst for the Hydrogen Evolution Reaction. *Angew. Chem., Int. Ed.* **2015**, *54*, 6325−6329.

(37) Fujii, R.; Gotoh, Y.; Liao, M. Y.; Tsuji, H.; Ishikawa, J. Work Function Measurement of Transition Metal Nitride and Carbide Thin Films. *Vacuum* **2006**, *80*, 832−835.

(38) Jiang, P.-C.; Lai, Y.-S.; Chen, J. S. Dependence of Crystal Structure and Work Function of WNx Films on the Nitrogen Content. *Appl. Phys. Lett.* **2006**, *89*, 122107.

(39) Wang, X.; Choi, S. I.; Roling, L. T.; Luo, M.; Ma, C.; Zhang, L.; Chi, M.; Liu, J.; Xie, Z.; Herron, J. A.; Mavrikakis, M.; Xia, Y. Palladium-Platinum Core-Shell Icosahedra with Substantially Enhanced Activity and Durability Towards Oxygen Reduction. *Nat. Commun.* **2015**, *6*, 7594.

(40) Long, N. V.; Duy Hien, T.; Asaka, T.; Ohtaki, M.; Nogami, M. Synthesis and Characterization of Pt−Pd Alloy and Core-Shell Bimetallic Nanoparticles for Direct Methanol Fuel Cells (DMFCs): Enhanced Electrocatalytic Properties of Well-Shaped Core-Shell Morphologies and Nanostructures. *Int. J. Hydrogen Energy* **2011**, *36*, 8478−8491.

(41) Hendon, C. H.; Hunt, S. T.; Milina, M.; Butler, K. T.; Walsh, A.; Román-Leshkov, Y. Realistic Surface Descriptions of Heterometallic Interfaces: The Case of TiWC Coated in Noble Metals. *J. Phys. Chem. Lett.* **2016**, *7*, 4475−4482.

(42) Hammer, B.; Norskov, J. K. Theoretical Surface Science and Catalysis - Calculations and Concepts. *Adv. Catal.* **2000**, *45*, 71−129.

(43) Hammer, B.; Norskov, J. K. Why Gold is the Noblest of All the Metals. *Nature* **1995**, *376*, 238−240.

(44) Wartnaby, C. E.; Stuck, A.; Yeo, Y. Y.; King, D. A. Microcalorimetric Heats of Adsorption for CO, NO, and Oxygen on Pt{110}. *J. Phys. Chem.* **1996**, *100*, 12483−12488.

(45) Ertl, G.; Neumann, M.; Streit, K. M. Chemisorption of CO on the Pt(111) Surface. *Surf. Sci.* **1977**, *64*, 393−410.

(46) Wilken, T. R.; Morcom, W. R.; Wert, C. A.; Woodhouse, J. B. Reduction of Tungsten Oxide to Tungsten Metal. *Metall. Trans. B* **1976**, *7*, 589−597.

(47) Contreras, A. M.; Grunes, J.; Yan, X. M.; Liddle, A.; Somorjai, G. A. Fabrication of 2-Dimensional Platinum Nanocatalyst Arrays by Electron Beam Lithography: Ethylene Hydrogenation and CO-Poisoning Reaction Studies. *Top. Catal.* **2006**, *39*, 123−129.

(48) Ravel, B.; Newville, M. ATHENA, ARTEMIS, HEPHAESTUS: Data Analysis for X-Ray Absorption Spectroscopy Using IFEFFIT. *J. Synchrotron Radiat.* **2005**, *12*, 537−541.

(49) Kresse, G.; Furthmüller, J. Efficient Iterative Schemes for Ab Initio Total-Energy Calculations Using a Plane-Wave Basis Set. *Phys. Rev. B: Condens. Matter Mater. Phys.* **1996**, *54*, 11169−11186.

(50) Blöchl, P. E. Projector Augmented-Wave Method. *Phys. Rev. B: Condens. Matter Mater. Phys.* **1994**, *50*, 17953−17979.

(51) Hammer, B.; Hansen, L. B.; Nørskov, J. K. Improved Adsorption Energetics within Density-Functional Theory Using Revised Perdew-Burke-Ernzerhof Functionals. *Phys. Rev. B: Condens. Matter Mater. Phys.* **1999**, *59*, 7413−7421.

(52) Monkhorst, H. J.; Pack, J. D. Special Points for Brillouin-Zone Integrations. *Phys. Rev. B* **1976**, *13*, 5188−5192.

DOI: 10.1021/acscatal.9b01272